JOURNAL OF SOLID STATE CHEMISTRY 106, 237–252 (1993)

Microstructural and Thermal Characterization of Basic and Stoichiometric Lithium Phosphates, in Relation with Their Catalytic Activity

R. M. ROJAS,*,† J.L. MARTIN DE VIDALES,‡ A. DELGADO,§ AND J. V. SINISTERRA§

†*Instituto de Ciencia de Materiales, CSIC, Serrano 113, 28006 Madrid, Spain;*
‡*Facultad de Ciencias (C-6), Universidad Autónoma de Madrid, 28049 Madrid, Spain;*
and §*Departamento de Química Orgánica, Facultad de Farmacia, Universidad Complutense de Madrid, 28040 Madrid, Spain*

Received June 29, 1992; in revised form December 28, 1992; accepted December 29, 1992

A comparative study of basic and stoichiometric lithium phosphates has been carried out by thermal analysis, X-ray powder diffraction, and IR spectroscopy. Structural and microstructural characterization, carried out by the Rietveld method and a profile-fitting procedure for analysis of broadened X-ray diffraction peaks, reveal that, unlike stoichiometric material, basic lithium phosphate shows a very isotropic and homogeneous crystallite size distribution (mean size 225 Å). They are justified in terms of the synthesis procedure followed in the preparation of both phosphates. $\beta \rightarrow \gamma$-Li_3PO_4 transition in the catalyst is shifted up to 670°C and takes place as an exothermic reaction associated with a dramatic diminution of the surface area (45 to 2 m^2/g). The high surface area and the presence of solvated excess lithium cations, both being a consequence of the synthesis procedure, accounts for the catalytic activity shown by the nonstoichiometric lithium phosphate.

Introduction

Allyl alcohol constitutes a very useful product in petrochemistry, as a raw material for the synthesis of glycerine, 1,4 butanediol, and vinylic monomers for the polymer industry. Because of this, the isomerization reaction of propylene oxide to allyl alcohol is of high commercial interest. Basic lithium orthophosphate has been shown to be the most useful catalyst for this isomerization reaction (1–4). However, natural lithium phosphate (lithiophilyte) or synthetic stoichiometric Li_3PO_4 are poor catalysts for this reaction (5, 6). On the other hand, the active phase of the catalyst is not well determined. In our opinion, a deep knowledge of the structural features of nonstoichiometric, basic lithium phosphate seems to be essential in order to clarify these subjects. Having this in mind, a detailed comparative study, of both nonstoichiometric and stoichiometric lithium phosphate, has been undertaken. In this work we report on the results obtained from thermal analysis, X-ray powder diffraction, and infrared spectroscopy studies. They reveal some interesting peculiarities of the nonstoichiometric lithium phosphate that can contribute to a deeper characterization of the catalyst and to enlighten some aspects of the catalytic process.

Stoichiometric lithium phosphate has two polymorphs, β and γ. Both forms have hcp oxide ions with half the tetrahedral sites occupied by cations (7). The low-temperature form crystallizes in space group $Pmm2_1$ (No. 31) with $a_0 = 6.1150(10)$, $b_0 = 5.2394(11)$, and $c_0 = 4.8554(10)$ Å, $Z = 2$ (8). It transforms irreversibly at about 502°C

* To whom correspondence should be addressed.

0022-4596/93 $5.00

into the γ high-temperature form, also with orthorhombic symmetry, S.G. *Pmnb* (No. 62) and cell dimensions $a_0 = 6.1147$, $b_0 = 10.475$, $c_0 = 4.9228$ Å, $Z = 4$ (*8, 10*). The transformation $\beta \rightarrow \gamma\text{-}Li_3PO_4$ shows the characteristics of both continuous and martensitic transformation (*9*). The structure of the low-temperature form of Li_3PO_4 is similar to that of the high-temperature form and a derivative of it. Both Li and P are in tetrahedral coordination and are tightly held together by corner-sharing of the tetrahedra.

Experimental

Sample Preparation

The stoichiometric low-temperature form of Li_3PO_4 (hereafter named FOSCO3) has been prepared by the procedure described by Keffer *et al.* (*8*). Briefly, by neutralizing a slurry of 2 g of Li_2CO_3 in 50 ml of distilled water by slow addition of 18 ml of 1 *M* phosphoric acid. The reaction was carried out at 70–80°C and the suspension was maintained at this temperature for about 1 hr. The final solution had a pH value of 7.2. The precipitate was filtered off and washed three times with 20 ml of warm water (50°C) and dried at 140°C.

Nonstoichiometric lithium phosphate (hereafter named FOSLIOH) has been obtained by slow addition (80 ml/hr) of 1000 ml of 1 *M* phosphoric acid to a saturated solution of $LiOH \cdot H_2O$ (126 g in 1250 ml water). The reaction was carried out at 40–50°C. The pH value of the final solution was 11.6. The precipitate, after filtering, was washed 5 times with 1000 ml of warm water (50°C) and dried at 140°C.

Four batches (8 g) of this product were suspended in a saturated solution of $LiOH \cdot H_2O$ (25 g in 250 ml water) for 12, 24, 48, and 84 hr. The suspensions were stirred and the temperature was kept at 50°C during the entire period. The precipitates were washed and dried in the method described above. The so-obtained products are named FOS12, FOS24, FOS48, and FOS84 respectively. All reactions were carried out in open air.

Methods

X-ray powder diffraction diagrams were recorded in a Siemens D-501 goniometer with monochromatized Cu$K\alpha$ ($\lambda = 1.54184$ Å) radiation. Diagrams were recorded in the step scanning mode, with a 0.02°(2Θ) step scanning and 2 sec counting time. Powder diffraction diagrams for structural refinements were recorded between 15° and 140°(2Θ), with a 0.04°(2Θ) step scanning and 10 sec counting time. Divergence slits located in the incident beam were selected to ensure complete illumination of the specimen surface at 12°(2Θ). To minimize preferred orientation effects, a sideloading sample holder was used. The samples were repacked and rerun twice at 0.04°(2Θ) step scan and 2 sec counting time, to check for evidence of preferred orientation. Some changes in the intensity of the (002) peaks were noticed between the two data sets, suggesting that preferred orientation can be significant along this direction. All X-ray experiments were carried out at 20 ± 1°C. Data collection parameters for both samples are gathered in Table I.

TABLE I

X-RAY DIFFRACTION DATA-COLLECTION PARAMETERS

Radiation	Cu$K\alpha$ ($\lambda = 0.154184$ nm)
Wavelengths	$\lambda_1 = 0.154060$ nm, $\lambda_2 = 0.15443$ nm
Detector	Scintillation
Monocromator	Graphite (diffracted beam)
Slits	
Primary	1°
Receiving	0.15°
Soller	Incident, diffracted
Scan	
Range (°2Θ)	15–140
Step size (°2Θ)	0.04
Time/step (sec)	10
Temperature (°C)	20 ± 1
Bragg reflections	360 (2 × 180, Kα1-Kα2 radiation)
Intensities (counts)	
FOSCO3 Sample	
Background intensities	140–220
Maximum peak intensity	16334
FOSLIOH Sample	
Background intensities	150–200
Maximum peak intensity	5778

TABLE II

ANALYTICAL AND TEXTURAL DATA OF β-FOSLIOH, FOS24, FOS48, AND β-FOSCO3 SAMPLES

Sample	d_p (Å)	%P	%Li	Li/P (ratio)	S_{area} (m^2/g)	ΣV_p (cm^3/g)
β-FOSLIOH	875	23.4	20.1	3.8	43	0.83
FOS24	676	22.0	21.3	4.3	37	0.62
FOS48	574	20.1	20.5	4.5	27	0.62
β-FOSCO3	185	27.9	14.4	2.3	2	0.02

Differential thermal analysis (DTA) and thermogravimetric (TG) curves were simultaneously recorded in a Stanton STA 781 thermal analyzer at $15°C \cdot min^{-1}$ heating rate, both in air and nitrogen flow ($50 ml \cdot min^{-1}$), with α-Al_2O_3 as reference. About 20 mg of sample was used in each run. IR spectra of solids were recorded in the 4000–200 cm^{-1} range in a Nicolet 20SXC spectrometer, in KBr discs.

Lithium and phosphorus contents were determined by atomic absorption spectrometry, using a Perkin-Elmer 603 spectrometer. Surface area (S_{area}), accumulated pore volume (ΣV_p) and pore average diameter (d_p) of materials were determined with a Carlo-Erba Sorptomatic 1400 instrument. Analytical and textural data are gathered in Table II.

Catalytic isomerization of propylene oxide was carried out in a pulsed microreactor linked to a gas chromatograph Shimadzu GC14A (*12*). The optimum experimental conditions were selected as follows: reaction temperature 275°C, carrier gas flow (N_2) $30 ml \cdot min^{-1}$ and FID temperature 250°C. The chromatograph program was: initial temperature 100°C, hold for 4 min and then heated up to 140°C at $10°C \cdot min^{-1}$ heating rate. The column was a 3 m × $\frac{1}{8}$ inch TCEP on chromosorb PAW 80/100.

Results and Discussion

Thermal Analysis, IR, and X-Ray Powder Diffraction Studies

DTA and TG curves of lithium phosphate (FOSCO3) are presented in Fig. 1. The DTA curve shows a moderately endothermic effect with a peak temperature of 475°C, as well as a rather small and continuous weight loss (≈2%) from 280°C up to the limit temperature (870°C). The endotherm peak corresponds to the nonreversible $\beta \rightarrow \gamma$ transformation already described (*8, 10*). In fact, X-ray powder diagrams (Figs. 2a and 2b) recorded with the sample heated at temperatures below and after the peak, correspond with β and γ forms of Li_3PO_4 respectively

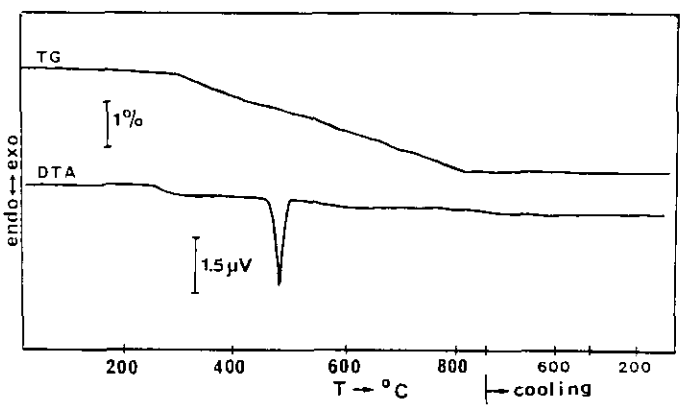

FIG. 1. Differential thermal analysis (DTA) and thermogravimetric (TG) curves recorded on stoichiometric Li_3PO_4 (FOSCO3).

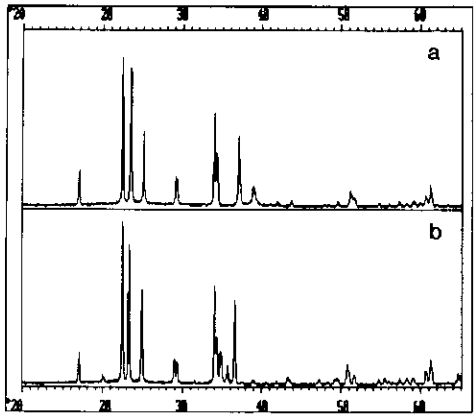

FIG. 2. X-ray powder diffraction diagrams recorded on FOSCO3 heated at (a) 450°C, β-phase; and (b) 600°C, γ-phase.

(25-1030 and 15-670 Powder Diffraction File cards).

Thermograms recorded on nonstoichiometric lithium phosphate sample (FOSLIOH) are depicted in Fig. 3. They show some very interesting and striking features. The most remarkable one being that the endothermic effect mentioned above has disappeared. Instead of that, a very strong needle-shaped exothermic effect is observed in the temperature range 628–688°C, with T_{max} = 671°C. On the other hand, the TG curve shows that the sample experiences an overall weight loss of 5.93% between 54°C and 860°C, that occurs in three consecutive steps.

X-ray powder diffraction diagrams recorded on FOSLIOH sample before and after the exothermic peak are shown in Figs. 4a and 4b respectively. The diagram shown in Fig. 4a is identical to the one recorded on FOSLIOH without being submitted to any thermal treatment. It agrees with the one shown for β-Li_3PO_4 (Fig. 2a), although some differences have to be taken into account, such as the broadening of the diffraction peaks and the relative intensity of some of the diffraction maxima. An X-ray powder diagram recorded on FOSLIOH heated at 700°C (Fig. 4b) is identical to the one reported for γ-Li_3PO_4 (Fig. 2b).

Having in mind the nonstoichiometric composition of FOSLIOH, and in order to investigate the possibility of increasing its catalytic activity, batches of the catalyst were left standing for several periods of time in a saturated solution of lithium hydroxide in open air.

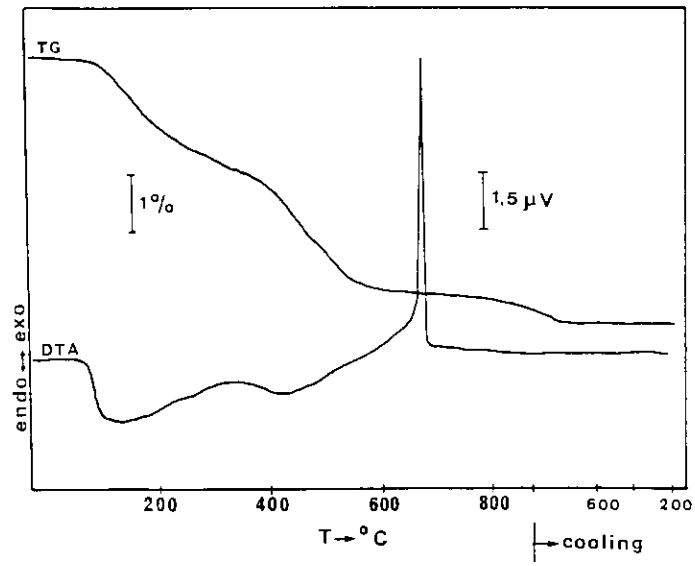

FIG. 3. DTA and TG curves recorded on FOSLIOH catalyst.

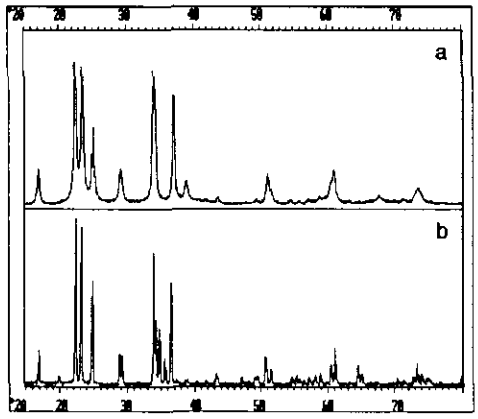

FIG. 4. X-ray powder diffraction diagrams recorded on FOSLIOH heated at (a) 600°C and (b) 700°C.

DTA and TG curves of FOS12 and FOS84 are shown in Figs. 5a and 5b respectively. DTA curves show neither the needle-shaped exothermic peak observed in FOSLIOH at 671°C nor the endothermic effect at 475°C shown by FOSCO3. However, the endothermic peak recorded at about 700°C and the exothermic effects observed in the DTA cooling curve recorded on FOS84 clearly reveal the presence of Li_2CO_3 in these materials. On the other hand, TG curves show a very well-defined step in the temperature range 710–860°C, that corresponds to the melting with decomposition of Li_2CO_3 (*11*). In Fig. 6, thermograms recorded on Li_2CO_3

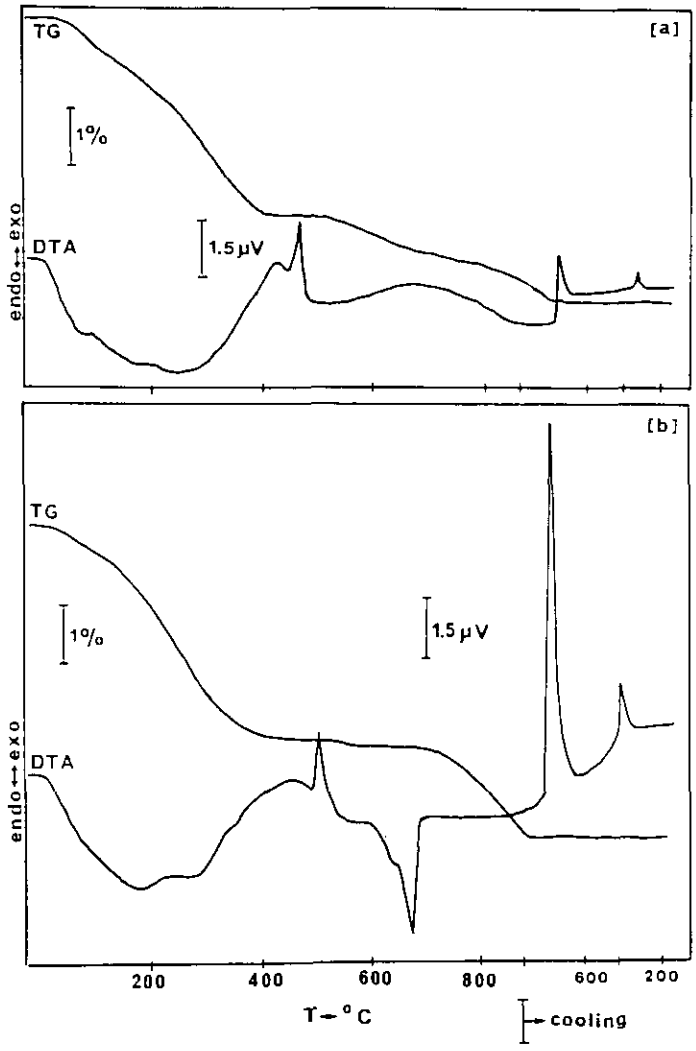

FIG. 5. DTA and TG curves of (a) FOS12, and (b) FOS84.

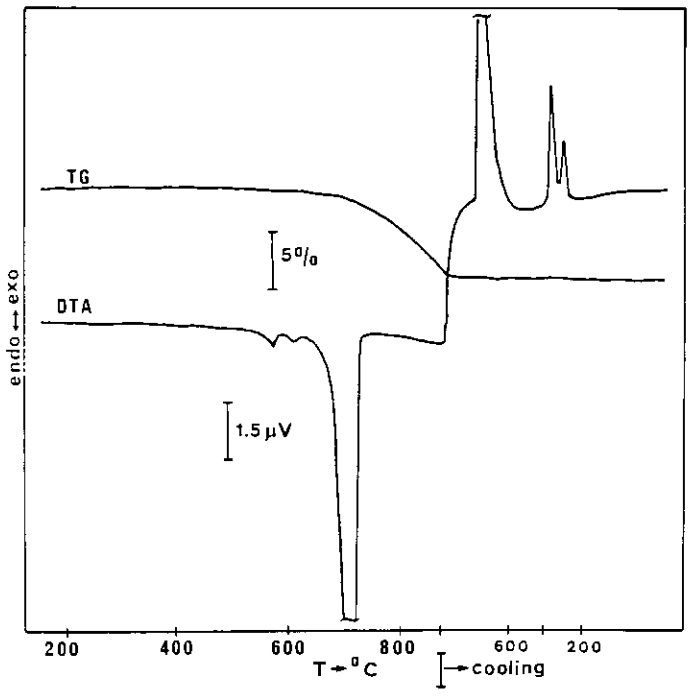

FIG. 6. DTA and TG curves recorded on Li_2CO_3 in N_2 flow (50 ml · min^{-1}) and 10°C · min^{-1} heating rate.

are presented. The two small endothermic peaks that appear in the DTA heating curve at about 575°C are clearly evident in the cooling DTA trace. Diffraction maxima of the latter compound have been identified in X-ray powder diffraction diagrams recorded on these four samples (Figs. 7a–7d). In the IR spectra recorded on FOS12 and FOS84 (Fig. 8a), the most intense bands of Li_2CO_3 at 1501, 1443, 858, and 497 cm^{-1} are observed (Fig. 8c), (*13*). The IR spectrum of FOSLIOH shows a poorly defined shoulder at 1501 cm^{-1} and a small increase of the absorption band at 1443 cm^{-1}, compared to the stoichiometric FOSCO3 (Fig. 8b). It could indicate the presence of a very small amount of Li_2CO_3 in FOSLIOH.

Structure Refinements

The least-squares structure refinements were undertaken with the full-profile, Rietveld-type, program DBWS-9006PC (release 31/8/91), prepared by Sakthivel and Young (*14*) for IBM-AT compatible microcomputers. This program can accept X-ray data obtained from a conventional diffractometer, because it allows the simultaneous refinement of two wavelengths (i.e., α_2 and α_1) if their intensity ratio is known (0.5 in the present case). The weight assigned to the intensity observed at each step "i" in the pattern is $W_i = 1/Y_{io}$, and the function minimized in the least-squares procedures is $\sum_i W_i \cdot (Y_{io} - Y_{ic})^2$, where Y_{io} and Y_{ic} are the observed and calculated intensities at each point i in the pattern, including the background intensity points. The observed X-ray powder diffraction profile for FOSCO3 indicates that most of the peaks in the pattern are relatively sharp (FWHM $\approx$0.17°(2Θ) at 16.90°(2Θ), $\approx$0.26°(2Θ) at 51.00°(2Θ), $\approx$0.40°(2Θ) at 100.00°(2Θ), and $\approx$0.58°(2Θ) at 135°(2Θ)). A pseudo-Voigt function was used for the representation of the profile. In this function, the parameter η is a linear function of Gaussian (G) and Cauchy (L) fractions: $\eta L + (1 - \eta)G$, and can be refined as a function of 2Θ where the

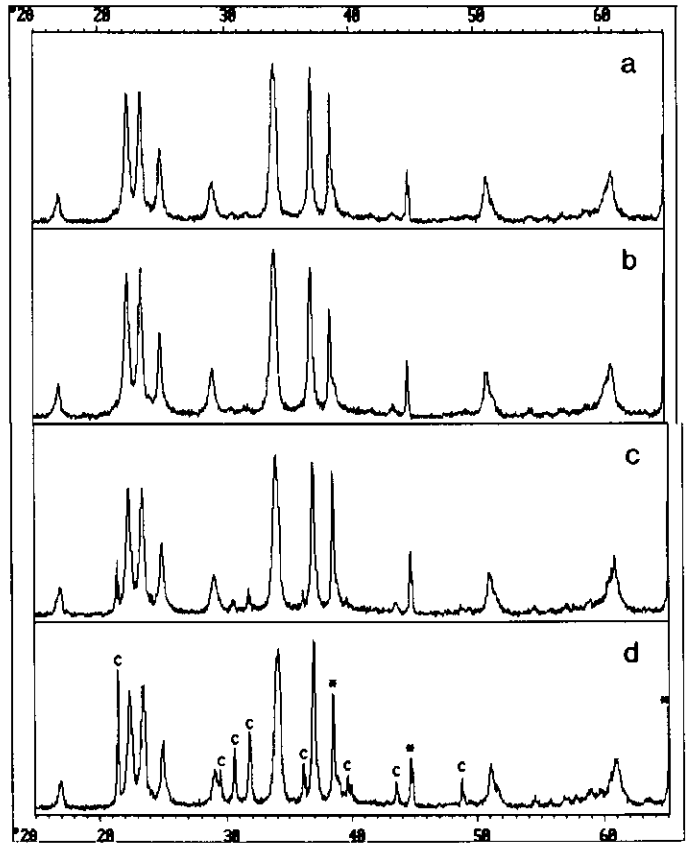

FIG. 7. X-ray powder diffraction diagrams recorded on (a) FOS12, (b) FOS24, (c) FOS48, and (d) FOS84. Maxima with (*) are aluminum from the sample holder; those with a "c" correspond to Li_2CO_3 diffraction lines.

refinable variables are NA and NB: $\eta = NA + NB \cdot (2\Theta)$. When $\eta = 0$, this function is a pure Gaussian ($1 - \eta = 1$) and for $\eta = 1$ is a pure Cauchy function; so, $(1 - \eta)$ value indicates the Gaussian fraction.

However, the observed X-ray powder diffraction profile for FOSLIOH shows that peaks in the pattern are broader (FWHM $\approx$ 0.42°(2Θ) at 16.90°(2Θ), 0.43°(2Θ) at 51.00°(2Θ), $\approx$1.16°(2Θ) at 100.00°(2Θ), and $\approx$2.70°(2Θ) at 135°(2Θ)). In this case, after trying pseudo-Voigt and Pearson VII functions, a pure Lorentzian (Cauchy) function was selected.

In both samples, FOSCO3 and FOSLIOH, the refined quantities are: C-scale factor, 2Θ zero shift parameter, and a peak full width at half maximum (FWHM) function described by the usual quadratic form

$$\mathrm{FWHM}^2 = U \cdot \tan^2(\Theta) + V \cdot \tan \Theta + W,$$

where U, V, and W are the refined parameters; the peak asymmetry parameters; the unit cell constants a, b, and c; and the fractional atomic coordinates. Finally, the overall isotropic thermal parameter B, was also refined.

The background intensity y_{bi} at the ith step was refined from the refinable background function $y_{bi} = \sum_{m=0}^{3} B_m \cdot [(2\Theta_i/\mathrm{BKPOS}) - 1]^m$, where BKPOS is the origin of the polynomial for background, being 1°(2Θ) in these refinements. The last variable to be refined is the preferred orientation factor

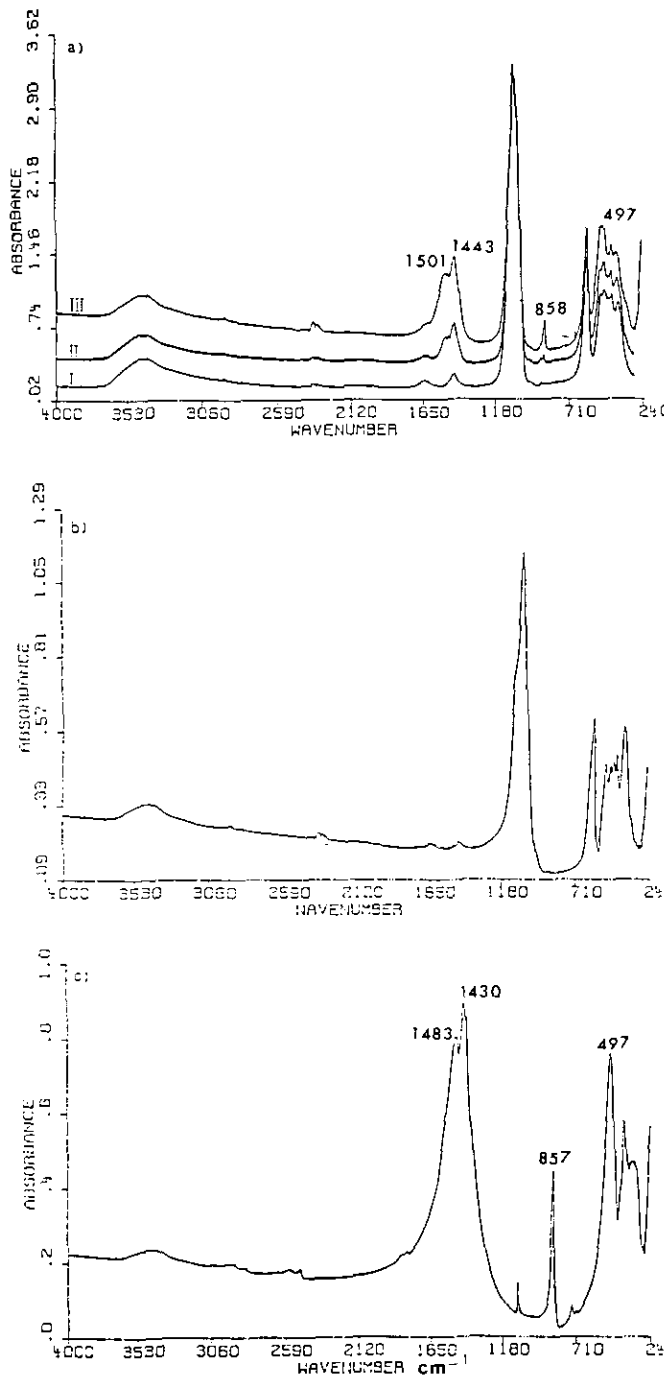

FIG. 8. Infrared spectra of (a) FOSLIOH (I), FOS12 (II), FOS84 (III); (b) FOSCO3; and (c) Li_2CO_3. Frequencies of the IR absorption bands discussed in the text have been indicated.

*G*1. Width of the calculated profile were 5 and 7 half-widths on either side of the peak position for FOSCO3 and FOSLIOH respectively.

The refinements were initiated using a = 6.1150, b = 5.2394, and c = 4.8554 Å (*8*), and an overall isotropic temperature factor B = 1.00 Å^2 for both structures. The initial values for scale factor and half-width parameters U, V, and W were estimated by inspection of the observed diffraction patterns. Initial fractional atomic coordinates were also taken from Keffer *et al.* (*8*). The complete set of results for the best-fit model are given in Tables III and IV. Figs. 9a and 9b shows a plot of the observed, calculated, and difference profiles for the two final refinements (FOSCO3 and FOSLIOH structures).

The quantities used to estimate the agreement between the observations and the model during the course of the Rietveld refinements were: R_p, R_{wp}, R_B, R_F, R_{exp}, and the goodness of fit (GF) = $|R_{wp}/R_{exp}|^2$ (*14–16*).

The quantity minimized in a Rietveld refinement is the weighted profile R-value, R_{wp}, but its numerical value may be misleading. Thus, it is not the value of the minimum reached in the weighted profile R-factor, but the structure parameter set (R_B and R_F) obtained from the minimum value, which are the most significant (*15*). After Rietveld refinement, the obtained agreement indexes were R_B = 9.67, R_F = 10.66, and R_B = 10.35, R_F 10.52 for FOSCO3 and FOSLIOH, respectively. Moreover, the goodness of fit is better for FOSLIOH (GF = 2.31) than the one obtained for FOSCO3 (GF = 2.91). In FOSCO3 sample, these discrepancies could be related with the presence of defects, crys-

TABLE III

FINAL RIETVELD REFINEMENT PARAMETERS FOR FOSCO3

Profile function used	pseudo-Voigt	
Width of calculated profile (in units of FWHM)	5	
Space group	$Pmn2_1$	
Cell dimensions	a = 6.1165(3) Å	
	b = 5.2400(3) Å	
	c = 4.8637(2) Å	
Volume	155.88(6) Å^3	
Overall isotropic temperature factor	B = 1.55(6) Å^2	
ETA pseudo-Voight mixing coeff.	NA = 0.45(3)	
	NB = 0.004(1)	
Asymmetry parameter	P = 0.038(2)	
Preferred orientation coeff.	$G1$ = 0.111(4), 002 direction.	
FWHM function parameters	U = 0.04(2)	
	V = 0.10(1)	
	W = 0.010(2)	
Zero-shift	−0.004(1)	
Scale factor	0.165(1)E-02	
Parameters	17	
Agreement indexes	R_p	11.61
	R_{wp}	15.16
	R-expected	5.21
	R-Bragg	9.67
	R-structure factors	10.66
	The goodness of fit (GF)	2.91

Note. Values in parentheses are estimated standard deviations in the last place. Fractionary coordinates were constrained those from Keffer *et al.* (8).

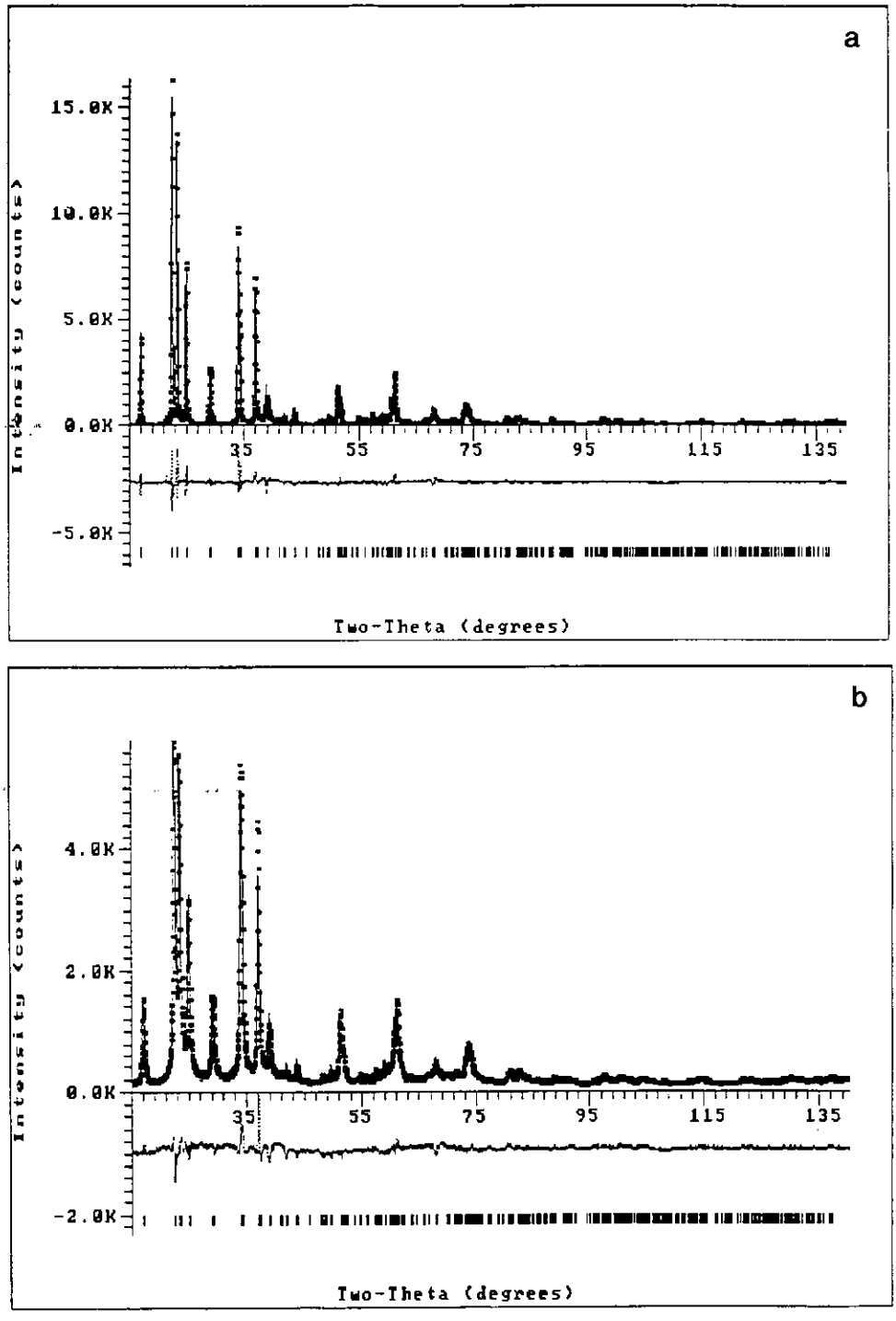

FIG. 9. The final Rietveld refinement plots of (a) FOSCO3 and (b) FOSLIOH from the Siemens D-501 data set. The upper trace shows the observed data as squares (■) and calculated pattern is shown by the solid line. The lower trace is a plot of the difference: observed minus calculated. The vertical markers show positions calculated for Bragg reflections.

TABLE IV

FINAL RIETVELD REFINEMENT PARAMETERS FOR FOSLIOH

Profile function used	Lorentzian	
Width of calculated profile (in units of FWHM)	7	
Space group	$Pmn2_1$	
Cell dimensions	a = 6.1220(7) Å	
	b = 5.2531(6) Å	
	c = 4.8738(5) Å	
Volume	156.74(4) Å^3	
Overall isotropic temperature factor	B = 2.35(8) Å^2	
Asymmetry parameter	P = −0.009(4)	
Preferred orientation coeff.	$G1$ = 0.121(4), 002 direction.	
FWHM function parameters	U = 0.88(13)	
	V = −0.41(8)	
	W = 0.19(1)	
Zero-shift	0.076(3)	
Scale factor	0.169(1)E-02	
Parameters	17	
Agreement indexes	R_p	8.97
	R_{wp}	12.01
	R-expected	5.21
	R-Bragg	10.35
	R-structure factors	10.52
	The goodness of fit (GF)	2.31

Note. Values in parentheses are estimated standard deviations in the last place. Fractionary coordinates were constrained those from Keffer *et al.* (8).

tallites of markedly anisotropic shapes and/or lattice strains. Obviously, and in order to assess accurately the quality of the refined structure, some other criteria must be used along with the agreement indexes discussed above. Probably, the most important test of a structure refinement is whether occupancy factors, bond distances, and angles have reasonable chemical sense (*16*). Since the fractional atomic coordinates were constrained to the Keffer values (*8*), our refined bond distances and angles only show slight differences from these, being caused by the slightly different values of our refined unit cell parameters (Tables III and IV). The R-values discussed above indicate a relatively good agreement between the observations and the model.

Refined unit cell parameters are as follows: a = 6.1165(3), b = 5.2400(3), and c = 4.8637(2) Å for the FOSCO3 structure and a = 6.1220(7), b = 5.2531(6), and c = 4.8738(5) Å for FOSLIOH structure. These results show a difference of ≈0.01 Å for a, b, and c cell-parameters between FOSCO3 and FOSLIOH structures. According to cell-parameters obtained from single crystal studies (*8*), a = 6.1150(10), b = 5.239(11), and c = 4.8554(10) Å, our results indicate a significant deviation of all cell-parameters for FOSLIOH, but also for c parameter in FOSCO3 structure.

In the FOSCO3 structure, discrepancy may be related to the presence of strains in ($h0l$), ($0kl$) and ($00l$) directions, whereas in the FOSLIOH structure it might be caused by defects related to the crystallite size; the pure Lorentzian function used during the Rietveld refinement clearly shows the small contributions due to strain defects (*17*).

Microstructural Characterization

To fit the selected experimental peaks, the program FITCONV (*18*) was used. This program uses pseudo-Voigt function PV(2Θ) convoluted with an exponential function $A(2\Theta)$ accounting for asymmetry, while the background (bkg) is supposed to be linear in the selected 2Θ region:

$$I(2\Theta) = \mathrm{PV}(2\Theta) * A(2\Theta)$$

$$\mathrm{PV}(2\Theta) = I_p[(1-\eta)(1+x^2)^{-1} + \eta(\exp(x^2 \ln 2)]$$

$$A(2\Theta) = \exp[-a|2\Theta_m - 2\Theta_o|\tan(2\Theta_o)],$$

where $x = (2\Theta - 2\Theta_o)/w$, $2\Theta_o$ is the peak maximum position, $2w$ is the FWHM, I_p is the intensity at the $K\alpha_1$ maximum, $(1-\eta)$ is the Gaussian content, and a is the asymmetry parameter. A statistical weight $1/(I(2\Theta))^{1/2}$ was adopted in the fitting procedure.

Peaks of a ZnO standard sample, obtained from thermal decomposition of $ZnCO_3$ heated at 950°C for 48 hr, was used to determine the instrumental and geometrical profile for the various angular ranges, as recommended by Langford *et al.* (*19*). The typical FWHM was 0.082 at 30°(2Θ) ($\eta = 0.42$).

Two different methods of peak profile analysis were used to obtain the crystallite size and microstrain: the Warren–Averbach method (WA) (*20, 21*) and the single peak analysis (SP) proposed by De Keijser *et al.* (*22, 23*).

In the WA method, it is assumed that the broadening due to size effects does not depend on the reflection order, while that due to microstrains does. Using two or more peaks of the same family it is possible to separate the two contributions, obtaining the rms microstrain distributions $\langle \varepsilon_L \rangle^{1/2}$ and the crystallite size distributions (*24*). Unfortunately, in the present case, the X-ray diffraction patterns of the both FOSCO3 and FOSLIOH do not present nonoverlapped second order diffraction peaks with clearly observable intensities, suitable to evaluate microstains, but it is possible to determine crystallite sizes very accurately.

However, the SP analysis uses a single peak, after correcting for the instrumental and geometrical profile by algebraic formulas. The method attributes the Cauchy component of the profile to the crystallite size effect, and the Gaussian component to the microstrain effect. In the WA method, this corresponds to assuming a constant microstrain distribution. For a Gaussian strain profile it has been shown that $e \approx \langle \varepsilon_L \rangle^2$ (*25*).

The analysis of the broadening was carried out on 110, 101, 011, 111, and 200 (Figs. 10a and 11a) and 210, 020, 002, 211, and 021

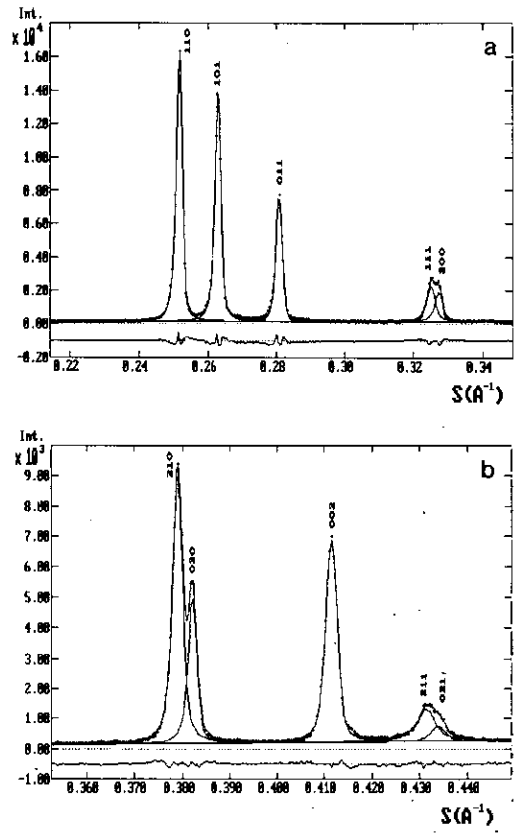

FIG. 10. Analysis by fitting procedure of the (a) 110, 101, 011, 111, and 200, and (b) 210, 020, 002, 211, and 021 orthorhombic reflections for FOSCO3 sample. The observed data and calculated pattern are shown by dots and solid line respectively. The lower trace is a plot of the difference: observed minus calculated.

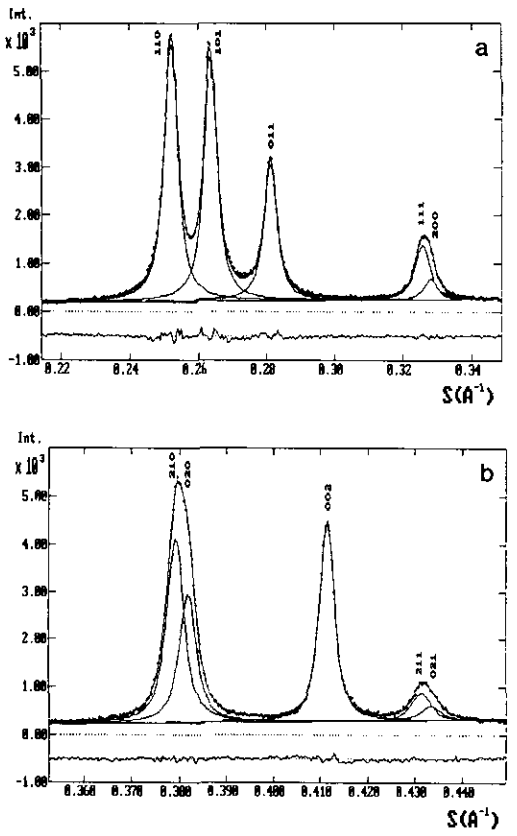

FIG. 11. Analysis by fitting procedure of the (a) 110, 101, 011, 111, and 200, and (b) 210, 020, 002, 211, and 021 orthorhombic reflections for FOSLIOH sample. The observed data and calculated pattern are shown by dots and solid line respectively. The lower trace is a plot of the difference: observed minus calculated.

reflections (Figs. 10b and 11b). Figs. 10a and 10b show the corresponding fitted peaks profile for FOSCO3 sample; the obtained reliability indexes, as defined by Enzo *et al.* (*18*), R_p and R'_p for the "pure" best fitted pseudo-Voigt functions ($K\alpha_1$ profiles), obtained by a convolutive optimization route were $R_p = 3.6$; $R'_p = 3.7$ and $R_p = 2.3$; $R'_p = 2.5$, respectively. Figs. 11a and 11b show the corresponding fitted peaks profiles for FOSLIOH sample. In these cases, the obtained reliability indexes R_p and R'_p for the "pure" best fitted pseudo-Voigt functions were $R_p = 2.6$; $R'_p = 2.9$ and $R_p = 2.3$; $R'_p = 2.6$, respectively.

Table V shows the FWHM ($2w$) and the Gaussian content ($1 - \eta$) for these 10 *hkl* reflections for both FOSCO3 and FOSLIOH samples. Table VI records the crystallite sizes deduced with the WA method from the Fourier transforms of the best-fitted profiles. Tables VI and VII show the parameters used to determine crystallite sizes (D) and microstains (e) from the single peak method. As it can be observed, the numerical agreement between the methods is not always satisfactory for the crystallite mean size of FOSCO3 sample, while the trend for FOSLIOH sample is quite similar. This disagreement for the more anisotropic sample (FOSCO3) is mainly due to the different hypotheses adopted by the two models. In fact it is not generally valid to attribute size effect to the Cauchy component and strain effect to the Gaussian component of XRD peaks as in the SP method. This can lead to wrong repartition of the peak broadening between size and strain, as shown by 011 ($\eta = 0.04$) and 211 ($\eta = 0.99$) peaks (Table VII) where the profiles are totally Gaussian and Cauchy, respectively. So, these two peaks are not taken into account in the SP analysis.

TABLE V

PARAMETERS OBTAINED BY THE BEST-FITTING PROCEDURES ON FOSCO3 AND FOSLIOH

			"Pure" pseudo-Voigt profiles			
			FOSCO3		FOSLIOH	
h	*k*	*l*	FWHM (°)	Gaussian content ($1 - \eta$)	FWHM (°)	Gaussian content ($1 - \eta$)
1	1	0	0.086	0.440	0.358	0.099
1	0	1	0.111	0.588	0.348	0.099
0	1	1	0.146	0.959	0.344	0.098
1	1	1	0.140	0.185	0.393	0.101
2	0	0	0.118	0.306	0.328	0.099
2	1	0	0.090	0.152	0.298	0.113
0	2	0	0.055	0.118	0.296	0.117
0	0	2	0.178	0.690	0.241	0.109
2	1	1	0.299	<0.001	0.378	0.292
0	2	1	0.251	0.791	0.383	0.117

TABLE VI

CRYSTALLITE SIZES ON Li_3PO_4 POWDERS (FOSCO3 AND FOSLIOH) OBTAINED BY THE CONVOLUTIVE ROUTE USING PSEUDO-VOIGT FUNCTIONS AND ASYMMETRY (WARREN–AVERBACH ANALYSIS ON THE BASIS OF FOURIER METHODS)

			FOSCO3		FOSLIOH	
h	k	l	D_{eff} (Å)	$\langle D\rangle_v$ (Å)	D_{eff} (Å)	$\langle D\rangle_v$ (Å)
1	1	0	596	782	112	166
1	0	1	536	639	110	166
0	1	1	[a]	[a]	117	174
1	1	1	304	442	103	154
2	0	0	393	549	126	187
2	1	0	469	689	139	206
0	2	0	751	1113	140	208
0	0	2	394[a]	421[a]	173	257
2	1	1	132	200	125	175
0	2	1	[a]	[a]	110	163

[a] Intractable cases due to the high gaussian content (see Table VII). These sizes cannot be resolved because of the absence of two or more peaks of the same family, since it is not possible to separate the two contributions, i.e., size and strain effects.

All the above indicated results obtained from the profile peaks convolution point out the influence of the synthesis procedure in the catalytic activity of lithium phosphate. The catalytic activity being therefore closely related with the microstructural features shown by FOSLIOH sample.

The FOSLIOH catalyst, obtained from H_3PO_4 and lithium hydroxide saturated solution in a highly alkaline medium (pH = 11.6), shows a very homogeneous crystallite size distribution (mean size ≈ 225 Å) and a microstrain distribution between 1.04 and 2.54E-03. On the other hand, the nonactive FOSCO3 phase, obtained from H_3PO_4 and lithium carbonate (pH = 7.2) is highly anisotropic with mean size distribution of 690, 1200, and 980 Å, along *a*, *b*, and *c* directions and significantly microstrained along the *a* and *c* directions, compared with *b* direction (see Tables VII and VIII).

The important microstructural differences observed between both FOSLIOH and FOSCO3 give account for the catalytic activity of FOSLIOH, that is closely related with the high surface area of the catalyst (see Table II).

Catalytic Activity

The catalytic activity of the solids is gathered in Table IX. It can be observed that only the FOSLIOH sample gives isomerization of propylene oxide (PO) to allyl alcohol

TABLE VII

PARAMETERS USED TO DETERMINE CRYSTALLITE SIZES (D) AND MICROSTRAINS (e) FROM THE SINGLE PEAK METHOD SAMPLE FOSCO3

h	k	l	$2w$	η	β	$\phi = 2w/\beta$	β_L	β_G	D (Å)	$e\cdot10^{-3}$
1	1	0	0.086	0.56	0.1155	0.7418	0.0794	0.0573	1134	1.26
1	0	1	0.111	0.41	0.1414	0.7855	0.0775	0.0865	1043	1.83
0	1	1[a]	0.146	0.04	0.1584	0.9215	0.0111	0.1515	8150	2.99
1	1	1	0.141	0.82	0.2075	0.6770	0.1830	0.0606	499	1.02
2	0	0	0.118	0.69	0.1669	0.7063	0.1328	0.0656	687	1.10
2	1	0	0.090	0.85	0.1344	0.6694	0.1214	0.0352	761	0.50
0	2	0	0.055	0.88	0.0831	0.6618	0.0769	0.0189	1202	0.27
0	0	2	0.178	0.31	0.2174	0.8187	0.0951	0.1515	980	1.98
2	1	1[a]	0.299	0.99	0.4695	0.6368	0.4670	0.0079	200	<0.01
0	2	1	0.251	0.21	0.2937	0.8545	0.0922	0.2310	1017	2.84

Note. β is the integral breadth. Subscripts "L" and "G" stand for Cauchy and Gaussian components, respectively. The ratio $\phi = 2w/\beta$, when is 0.63362 the profile is fully Cauchy and when $\phi = 0.93949$, it is fully Gaussian (*26*).

[a] Wrong repartition of the peak broadening between size and strain due to the totally Gaussian (011) and Cauchy (211) peak profiles (see text).

TABLE VIII

PARAMETERS USED TO DETERMINE CRYSTALLITE SIZES (D) AND MICROSTRAINS (e) FROM THE SINGLE PEAK METHOD SAMPLE FOSLIOH

h k l	$2w$	η	β	$\phi = 2w/\beta$	β_L	β_G	D (Å)	$e \cdot 10^{-3}$
1 1 0	0.358	0.90	0.5444	0.6576	0.5101	0.1126	176	2.48
1 0 1	0.348	0.90	0.5292	0.6576	0.4958	0.1095	182	2.30
0 1 1	0.344	0.90	0.5233	0.6574	0.4906	0.1077	184	2.12
1 1 1	0.393	0.90	0.5972	0.6580	0.5589	0.1247	186	2.10
2 0 0	0.328	0.90	0.4988	0.6576	0.4675	0.1120	195	1.87
2 1 0	0.298	0.89	0.4510	0.6607	0.4190	0.1002	220	1.43
0 2 0	0.296	0.88	0.4474	0.6616	0.4142	0.1014	220	1.44
0 0 2	0.241	0.89	0.3652	0.6598	0.3400	0.0796	273	1.04
2 1 1	0.378	0.71	0.5379	0.7027	0.4338	0.2051	215	2.54
0 2 1	0.383	0.88	0.5789	0.6616	0.5359	0.1312	175	1.61

Note. β is the integral breadth. Subscripts "L" and "G" stand for Cauchy and Gaussian components, respectively. The ratio $\phi = 2w/\beta$, when is 0.63662 the profile is fully Cauchy and when $\phi = 0.93949$, it is fully Gaussian (26).

(AA), 44% yield. The other solids give very poor yields in AA (<3.22%) and FOSCO3 is not active in the isomerization to AA. Therefore, only basic lithium phosphate is active.

Conclusions

Studies carried out on basic and stoichiometric lithium phosphates by thermal analysis, X-ray powder diffraction, and IR spectroscopy lead to results that can account for the catalytic activity shown by nonstoichiometric lithium phosphate and furnish some information about the active catalytic sites.

TABLE IX

CATALYTIC ACTIVITY MEASURED AS ISOMERIZATION PRODUCTS (%) FROM PROPYLENE OXIDE, CATALYZED BY SEVERAL SOLIDS (T = 275°C)

Catalyst	PO	AA	nPrOH	PA	AC
FOSLIOH	43.2	44.10	2.83	4.89	4.64
FOS12	87.8	2.47	3.51	2.13	3.61
FOS24	85.8	3.22	4.09	2.63	3.62
FOS48	85.1	2.93	3.77	2.13	4.60
FOS84	89.0	1.47	2.50	2.92	3.62
FOSCO3	91.7	1.31	0.21	4.22	2.02
Li_2CO_3	93.1	1.33	0.15	3.60	1.41

Note. PO, Propylene oxide; AA, Allyl alcohol; nPrOH, Propanol-1; PA, Propanal; AC, Acetone.

The X-ray peak profile analysis, carried out on basic, nonstoichiometric active, and stoichiometric nonactive lithium phosphate, reveals important differences between these two materials. While the active phase crystallites show a very isotropic and homogeneous size distribution, ≈225 Å, the nonactive material shows an important anisotropy, with a crystallite size distribution of ≈690, 1200, and 980 Å along the a, b, and c directions, respectively, as well as a very low surface area (2 m^2/g). These results can be explained in terms of the high pH value (11.6) of the final solution at which the lithium phosphate catalyst has been synthesized, rather higher than the isoelectic point of lithium phosphate. So, the electronegatively charged microcrystals could be homogeneously covered with an excess of solvated lithium cations, that would be the active sites of the catalyst. They also would prevent the crystals from growing, yielding a material with a rather high surface area (43 m^2/g) and a homogeneous crystallite size distribution. Consequently, the synthesis procedure determines the catalytic activity or nonactivity of lithium phosphate.

The needle-shaped exothermic effect ob-

served in the DTA curve of basic lithium phosphate is associated with the $\beta \rightarrow \gamma$ transition, that is hindered until the water molecules of solvated excess lithium cations are completely removed. In fact, once the weight (TG curve) stabilizes (see Fig. 3), the $\beta \rightarrow \gamma$ transition takes place and is accompanied by a dramatic diminution of the surface area (43 to 2 m^2/g).

On the other hand, when active FOSLIOH is left standing in a saturated lithium hydroxide solution, X-ray, thermal analysis and IR spectroscopy data indicate carbonation of the catalyst surface. The lithium carbonate deposited onto the catalyst surface blocks the active acid–basic sites, hindering any catalytic activity. In fact, FOS12 to FOS84 samples give very poor yields in the isomerization of propylene oxide to allyl alcohol (see Table IX). The slight diminution of the surface area (see Table II) cannot give account for the null catalytic activity of the carbonated species.

References

1. W. I. Denton, U.S. Patent 2,986,585 (1961).
2. H. B. Scholte, Eur. Patent 182, 446 (1985).
3. D. Hardy, U.S. Patent 4,842,666 (1982).
4. E. Danvic and S. Straja, *Can. J. Chem. Eng.* **67,** 137 (1981).
5. W. I. Denton, U.S. Patent 3,044,850 (1962).
6. J. B. Moffat, *Catal. Rev.* **18**(2), 199 (1978).
7. A. R. West, *in* "Solid State Chemistry and its Applications," p. 223, Wiley, New York (1984).
8. C. Keffer, A. Mighell, F. Mauer, H. Swanson, and S. Block, *Inorg. Chem.* **6,** 119 (1967).
9. C. Ibarra-Martínez, M. E. Villafuente-Castejón, and A. R. West, *J. Mater. Sci.* **20,** 812 (1985).
10. J. Zeeman, *Acta Crystallogr.* **13,** 863 (1960).
11. R. C. Mackenzie, *in* "Differential Thermal Analysis," Vol. I, p. 307, Academic Press, New York (1970).
12. A. Costa, P. Deya, J. V. Sinisterra, and J. M. Marinas, *Can. J. Chem* **58,** 1266 (1980).
13. W. B. White, *in* "The Infrared Spectra of Minerals" (V. C. Farmer, Ed.), Chap. 12, Mineralogical Society, London (1971).
14. A. Sakthivel and R. A. Young, "Users Guide to Programs DBWS-9006 and DBWS-9006PC for Rietveld Analysis of X-Ray and Neutron Powder Diffraction Patterns," School of Physics, Georgia Institute of Technology, Atlanta (1991).
15. R. A. Young and D. B. Wiles, *J. Appl. Crystallogr.* **15,** 430 (1982).
16. J. E. Post and D. L. Bish, *in* "Modern Powder Diffraction" (D. L. Bish and J. E. Post, Eds.), Chap. 9, The Mineralogical Society of America, Washington D.C. (1989).
17. S. A. Howard and R. L. Snyder, *Symp. Adv. Mater. Res.* **19,** 57 (1985).
18. S. Enzo, G. Fagherazzi, A. Benedetti and S. Polizzi, J. *Appl. Crystallogr.* **21,** 536 (1988).
19. J. I. Langford, D. Louër, E. J. Sonneveld, and J. W. Visser, *Powder Diffr.* **1,** 211 (1986).
20. B. E. Warren and B. L. Averbach, *J. Appl. Phys.* **21,** 595 (1950).
21. H. P. Klug and L. E. Alexander, "X-Ray Diffraction Procedures for Polycrystalline and Amorphous Materials," 2nd ed., Chap. 9, Wiley, New York (1974).
22. Th. H. De Keijser, J. I. Langford, E. Mittemeijer, and A. B. P. Vogels, *J. Appl. Crystallogr.* **15,** 308 (1982).
23. Th. H. De Keijser, E. Mittemeijer, and H. C. F. Rozendaal, *J. Appl. Crystallogr.* **16,** 309 (1983).
24. A. Guinier, "X-Ray Diffraction," p. 139, Freeman, San Francisco (1963).
25. R. Delhed, Th. H. De Keijser, E. Mittemeijer, and J. I. Langford, *Aust. J. Phys.* **41,** 213 (1988).
26. J. I. Langford, NBS Special Publication, *Accu. Powder Diffr.* **567,** 255 (1980).